Reconstruction of dielectrics from experimental data via a hybrid globally convergent/adaptive inverse algorithm

Larisa Beilina [*]   Michael V. Klibanov [†]

August 17, 2010

Abstract

The validity of a synthesis of a globally convergent numerical method with the adaptive FEM technique for a coefficient inverse problem is verified on time resolved experimental data. Refractive indices, locations and shapes of dielectric abnormalities are accurately imaged.

1 Introduction

In [9] a globally convergent numerical method for a Coefficient Inverse Problems (CIP) for a hyperbolic PDE was developed. Next, a two-stage numerical procedure was proposed in [10, 11, 12]. In this procedure the technique of [9] is used as the first stage. Next, the Adaptive Finite Element method (adaptivity below) is used as the second stage for the refinement. In [23] the first stage was verified on *blind* experimental data. The goal of the current publication is to demonstrate that the two-stage numerical procedure applied to the same experimental data can significantly improve imaging results compared with the first stage only. It was shown in [23] that the globally convergent stage can very accurately image locations and refractive indices of dielectric abnormalities. In addition, we demonstrate here that the adaptivity stage brings in the third important component: accurate images of shapes of those abnormalities. Since the theory was developed in [9]-[12], we do not derive new analytical results here. Instead we focus on the demonstration of the performance of that theory for our experimental data.

The main difficulty in applying the technique of [9]-[12] to our experimental data is caused by a huge discrepancy between these data and computationally simulated ones. The latter can be derived from a visual comparison of Figures 2-a) and 2-b) (below). Conventional data

[*]Department of Mathematical Sciences, Chalmers University of Technology and Gothenburg University, SE-42196 Gothenburg, Sweden, (`larisa@chalmers.se`)

[†]Department of Mathematics and Statistics University of North Carolina at Charlotte, Charlotte, NC 28223, USA, (`mklibanv@uncc.edu`)

denoising techniques, like, e.g. Fourier transform, Hilbert transform, spline interpolation, etc. provide only an insignificant help in our case. Hence, it is necessary to apply a *radically new* data pre-processing procedure as a crucial preliminary step. The goal of this step is to obtain acceptable boundary conditions, which are used in our numerical method. This procedure is based on the intuition only. The single justification of it is the accuracy of reconstruction results.

Our data pre-processing procedure consists of three stages. First two stages were described in [23] (they were new at that time). Hence, they are presented only briefly in this paper for the convenience of the reader. The third stage is new, since it is designed solely for the adaptivity technique. In particular, we describe a new rule for adaptive mesh refinements, which is much broader than the one used in [4]-[8],[10]-[12].

Our two-stage algorithm does not assume neither a knowledge of the background medium nor a knowledge of the presence/absence of small "sharp" abnormalities of our interest in the medium. It uses only the knowledge of the target coefficient outside of the medium of interest. Applications are in the detection of explosives, since their refractive indices usually are much higher that those of regular materials, see http://www.clippercontrols.com. Other procedures of solving CIPs, which do not rely on locally convergent algorithms, can be found in [2, 14, 20, 24, 26, 27].

An excellent accuracy of the blind reconstruction of both locations and refractive indices of dielectric abnormalities in [23] has led to the statement there that the globally convergent method of [9, 10] "is completely validated now". The same is true for a new mathematical model, which was proposed in [10, 23] due to an approximation of this numerical technique. That approximation is caused by the truncation of the large value $\overline{s}$ of the so-called pseudo frequency $s > 0$, which is the parameter of the Laplace transform of the original hyperbolic PDE. Such an approximation is likely inevitable due to tremendous challenges of the development of numerical methods for CIPs. Indeed, CIPs are both ill-posed and highly nonlinear. It is shown in [10, 23] that, from the analytical standpoint, the above truncation is neither better nor worse than the classical truncation of divergent asymptotic series in the Real Analysis.

To explain our need for the above two-stage procedure, we note that the number $1/\overline{s}$ cannot be made infinitely small in practical computations. At the same time, convergence estimates in global convergence theorems of [9, 10] depend on the small parameter $1/\overline{s}$. Hence, in practical terms, these theorems only guarantee that the solution obtained on the first stage is sufficiently close to the correct solution. However, they do not guarantee that the distance between computed and correct solutions can be made infinitely small. This opens the door for a refinement via a locally convergent technique. Indeed, the *key ingredient* for any such technique is a good first approximation for the solution. So, this approximation is provided on the globally convergent stage. It is shown below that, in the case of our experimental data, it is *crucial* that the good first guess for the solution taken from the globally convergent stage should be available for the adaptivity stage. On the other hand, it was demonstrated in section 8 of [23] that if a modified gradient method does not use the solution obtained on the first stage, then its performance is poor.

We have chosen the adaptivity because of our previous experience of [10]-[12]. It was shown in these references that the quasi-Newton method taken alone does not refine solution of the globally convergent stage. On the other hand it was also demonstrated in these references that a significant refinement is achieved if adaptive meshes are used. The same observation is presented in this paper. The adaptivity for CIPs was first proposed in [4, 5] and was developed further in [6, 8, 19]. It consists in minimizing either the Tikhonov functional [10]-[12] or the associated Lagrangian [4]-[8],[19] on a sequence of locally refined meshes in the FEM. Meshes are refined in such subdomains of the original domain, where *a posteriori* error analysis indicates the maximal error of the solution. That error analysis does not use a knowledge of the exact solution. Instead, one should know an upper bound of that solution, and such a bound should be imposed *a priori*, in accordance with the Tikhonov principle [31]. It was shown analytically in [12] that the mesh refinement indeed improves the accuracy of the regularized solution as long as the modulus of the gradient of the Tikhonov functional is not too small. However, as soon as it becomes too small, mesh refinements should be stopped. The latter has been consistently observed in [4]-[8], [10, 11], as well as in the current paper.

In section 2 we formulate both forward and inverse problems of our mathematical model and briefly outline both stages of our two-stage algorithm. In section 3 we describe the experimental setup. In section 4 the procedure of data simulation is described. This procedure is an integral part of our technique. In section 5 we describe how we pre-process our experimental data. In section 6 we present our imaging results. Discussion is presented in section 7.

2 Brief Outline of the Two-Stage Numerical Procedure

2.1 Statements of forward and inverse problems

As the forward problem, we consider the following Cauchy problem

$$\varepsilon_r(x)u_{tt} = \Delta u, \text{ in } \mathbb{R}^3 \times (0, \infty), \tag{1}$$
$$u(x, 0) = 0, u_t(x, 0) = \delta(x - x_0). \tag{2}$$

Here $\varepsilon_r(x)$ is the spatially variable dielectric constant (relative dielectric permittivity),

$$\varepsilon_r(x) = \frac{\varepsilon(x)}{\varepsilon_0}, \ \sqrt{\varepsilon_r(x)} = n(x) = \frac{c_0}{c(x)} \geq 1, \tag{3}$$

where ε_0 is the dielectric permittivity of the vacuum (which we assume to be the same as one in the air), $\varepsilon(x)$ is the spatially variable dielectric permittivity of the medium of interest, $n(x)$ is the refractive index of the medium of interest, $c(x)$ is the speed of the propagation of the EM field in this medium, and c_0 is the speed of light in the vacuum, which we assume to be the same as one in the air. We point out that it is the refractive index rather than the dielectric constant, which is measured in physics. The assumption $n(x) \geq 1$ means that the

3

speed of the EM field propagation in the medium does not exceed one in the air, which is reasonable.

Let $\Omega \subset \mathbb{R}^3$ be a convex bounded domain with the boundary $\partial\Omega \in C^3$. We assume that the coefficient $\varepsilon_r(x)$ of equation (1) is such that

$$
\begin{aligned}
\varepsilon_r(x) &\in (1, d], \varepsilon_r(x) = 1 \text{ for } x \in \mathbb{R}^3\backslash\Omega, &(4)\\
\varepsilon_r(x) &\in C^2\left(\mathbb{R}^3\right). &(5)
\end{aligned}
$$

The inequality $\varepsilon_r(x) \geq 1$ follows from (3). An upper estimate for the constant $d > 1$ is assumed to be known, although we do *not* assume that $d - 1$ is small.

Inverse Problem. *Suppose that the coefficient $\varepsilon_r(x)$ satisfies (4) and (5). Assume that the function $\varepsilon_r(x)$ is unknown in the domain Ω. Determine the function $\varepsilon_r(x)$ for $x \in \Omega$, assuming that the following function $g(x,t)$ is known for a single source position $x_0 \notin \overline{\Omega}$*

$$
u(x,t) = g(x,t), \forall (x,t) \in \partial\Omega \times (0, \infty). \quad (6)
$$

The assumption $\varepsilon_r(x) = 1$ for $x \in \mathbb{R}^3\backslash\Omega$ means that one has air outside of the medium of interest Ω. The question of uniqueness of this Inverse Problem is a well known long standing open question. It is addressed positively only if the function $\delta(x - x_0)$ above is replaced with a function $f(x)$ such that $f(x) \neq 0, \forall x \in \overline{\Omega}$. Corresponding uniqueness theorems were proven via the method of Carleman estimates [21, 22], also see a recent survey in [32]. Still, due to the applied aspect, numerical methods is worthy to develop, assuming that the uniqueness question is addressed positively.

Remark 2.1. In section 7 we discuss some discrepancies between our mathematical model and the reality. Since both stages of our two-stage numerical procedure were described in detail in our previous publications [9]-[12], we outline them only briefly in section 2, referring to these references for details. To save space, we do not specify functional spaces here. In the adaptivity we work only with standard piecewise linear finite elements.

2.2 The globally convergent stage

Consider the Laplace transform of the solution of the problem (1), (2),

$$
w(x,s) = \int_0^\infty u(x,t) e^{-st} dt, s \geq \underline{s} = const. > 0. \quad (7)
$$

Then $w(x,s) > 0$ for sufficiently large s. We consider the function $q(x,s) = \partial_s \left(s^{-2} \ln w(x,s)\right)$. Under certain conditions

$$
D_x^\alpha D_s^k \left(\frac{\ln w(x,s)}{s^2}\right) = O\left(\frac{1}{s^{k+1}}\right), s \to \infty, k = 0, 1; |\alpha| \leq 2. \quad (8)
$$

We obtain a nonlinear integral differential equation for the function q for $x \in \Omega, s \in (\underline{s}, \infty)$ with Volterra integrals in which the s-integration is carried out from an arbitrary $s \geq \underline{s}$ to

4

∞. One of the key features of this equation is that the unknown coefficient $\varepsilon_r(x)$ is not involved in it. The Dirichlet boundary condition at $\partial\Omega$ is generated by the function g in (6). If one would approximate the function q well, then one would approximate the function $\varepsilon_r(x)$ well via backwards computations. The main difficulty then is to solve the resulting Dirichlet boundary value problem for q. To do this, we first truncate those Volterra integrals at a large value $s := \overline{s} > \underline{s}$. However, we complement that truncation by the so-called "tail function" $V(x, \overline{s}) \approx \overline{s}^{-2} \ln w(x, \overline{s})$. The tail function is unknown. However, it is small for large $\overline{s}$ because of (8). Hence, the resulting equation for q contains two unknown functions: q and V. The reason why we can approximate both of them is that we treat them separately: while we approximate q via inner iterations, we approximate V via outer iterations.

To solve the resulting problem, we divide the interval $[\underline{s}, \overline{s}]$ into N small subintervals. We assume that the function q is constant with respect to s on each of those subintervals. As a result, we obtain N elliptic Dirichlet boundary value problems for functions $q_n(x)$, where n is the number of the subinterval. Because originally we had Volterra integrals with respect to s, we can solve these problems sequentially starting from q_1. Let $q_{n,k}$ be the approximation for q_n obtained on the inner iteration number k and $V_{n,k}(x)$ be the corresponding approximation for the tail. Then we find the corresponding approximation $\varepsilon_r^{(n,k)}(x)$ for the function $\varepsilon_r(x)$, solve the problem (1), (2) with $\varepsilon_r := \varepsilon_r^{(n,k)}(x)$, calculate the Laplace transform $w_{n,k+1}(x, \overline{s})$ via (7) for it and find a new approximation $V_{n,k+1}(x) := \overline{s}^{-2} \ln w_{n,k+1}(x, \overline{s})$ for the tail. Convergence criteria for this algorithm are described in [9, 10, 11, 12, 23]. In particular, in our computations for experimental data we use the criterion described in subsection 7.1 of [23].

2.3 The adaptivity

Let $T = const. > 0$. Denote $Q_T = \Omega \times (0, T)$, $S_T = \partial\Omega \times (0, T)$. Our goal now is to find such a function $\varepsilon_r(x)$, which minimizes the Tikhonov functional

$$E(\varepsilon_r) = \frac{1}{2} \int_{S_T} (u \mid_{S_T} - g(x, t))^2 dS_x dt + \frac{1}{2} \gamma \int_{\Omega} (\varepsilon_r - \varepsilon_r^{glob})^2 \ dx, \tag{9}$$

where ε_r^{glob} is the solution obtained on the globally convergent stage of our two-stage numerical procedure and γ is the regularization parameter. On the first step of the adaptivity we take the same mesh as one we have used for the globally convergent method. The first guess for iteration $\varepsilon_{r,0}(x) := \varepsilon_r^{glob}(x)$ is also taken on that mesh. On each follow up step of the adaptivity when mesh refinements are used, the first guess is again taken from the globally convergent stage. In doing so, values of the function ε_r^{glob} are linearly interpolated from the coarser grid on the finer grid.

Since $\varepsilon_r(x) = 1$ for $x \in \mathbb{R}^3 \backslash \Omega$, then, given the function $g(x, t) = u \mid_{\partial\Omega}$, one can uniquely determine the function $u(x, t)$ for $(x, t) \in (\mathbb{R}^3 \backslash \Omega) \times (0, T)$ as the solution of the boundary value problem for equation (1)-(2) with the Dirichlet condition $g(x, t)$ from (6). Hence, one can uniquely determine the normal derivative $p(x, t) = \partial_n u \mid_{S_T}$. Therefore, we consider the

5

solution of the following problem

$$\begin{aligned}
\varepsilon_r u_{tt} - \triangle u &= 0, \quad (x,t) \in Q_T, \\
u(x,0) = u_t(x,0) &= 0, \\
\partial_n u \mid_{S_T} &= p(x,t), \quad (x,t) \in S_T.
\end{aligned} \tag{10}$$

In addition, let the function $\lambda(x,t)$ be the solution of the following adjoint problem with the reversed time

$$\begin{aligned}
\varepsilon_r \lambda_{tt} - \triangle \lambda &= 0, \quad (x,t) \in Q_T, \\
\lambda(x,T) = \lambda_t(x,T) &= 0, \\
\partial_n \lambda \mid_{S_T} &= (g-u)(x,t), \quad (x,t) \in S_T.
\end{aligned} \tag{11}$$

We compute weak solutions of problems (10) and (11) via the FEM, see [4, 8] for details.

It was shown in [11, 12] that the Frechét derivative of the functional (9) is

$$E'(\varepsilon_r)(x) = \gamma \left(\varepsilon_r - \varepsilon_r^{glob} \right) - \int_0^T u_t \lambda_t dt, x \in \Omega \ .$$

Hence, we have to solve the following equation with respect to the function ε_r

$$E'(\varepsilon_r)(x) = 0, x \in \Omega. \tag{12}$$

In accordance with one of backbone principles of the regularization theory [31], we assume that there exists the unique exact solution ε_r^* of the original inverse problem. We also assume that there exists the unique minimizer $\varepsilon_{r,\gamma}$ of the functional $E(\varepsilon_r)$ in a small neighborhood of ε_r^*. So, $\varepsilon_{r,\gamma}$ is a regularized solution of our CIP. Consider a mesh in the domain Ω on which the Tikhonov functional $E(\varepsilon_r)$ is minimized. Let h be the maximal grid step size of this mesh. Suppose that there exists a unique minimizer $\varepsilon_{r,h}$ of the functional (9) on this mesh in a small neighborhood of ε_r^*. Let u_h and λ_h be corresponding FEM solutions of problems (10) and (11) respectively. *A posteriori* error analysis of [11] has shown that, in order to improve the accuracy of the calculation of $E(\varepsilon_{r,\gamma})$, one needs to refine mesh in neighborhoods of those points where the function $|E'(\varepsilon_{r,h})(x)|$, attains its maximal values. Here

$$|E'(\varepsilon_{r,h})(x)| = \left| \gamma \left(\varepsilon_{r,h} - \varepsilon_{r,h}^{glob} \right) - \int_0^T u_{ht} \lambda_{ht} dt \right|, x \in \Omega. \tag{13}$$

Here $\varepsilon_{r,h}^{glob}$ is the linear interpolation of the function ε_r^{glob} on this mesh.

Remarks 2.2:

1. Note that we mention here only the accuracy of the calculation of the functional $E(\varepsilon_{r,\gamma})$ rather than the accuracy of the reconstruction of the target coefficient. This is because of the ill-posedness of the original CIP, which is unlike the adaptivity for classic

6

well-posed forward problems [1, 28]. Nevertheless, it follows from the discussion on page 304 of [12] and Theorem 7.3 of [12] that, under certain additional conditions, this mesh refinement leads not only to a better accuracy of computing $E(\varepsilon_{r,\gamma})$ but also to a better accuracy of the calculation of the minimizer of (9) itself. This explains why the mesh refinement leads to the improvement of the image. Likewise, if considering the functional $E(\varepsilon_r)$ only on a finite dimensional space of piecewise linear finite elements, then uniqueness and existence of above minimizers $\varepsilon_{r,\gamma}$ and $\varepsilon_{r,h}$ follows from Theorems 3.1, 3.2 and 7.2 of [12].

2. In our experience of working with experimental data (13) is only an indicator. So, along with (13), we need to find additional criteria for mesh refinements. We found such based on our computational experience, see section 6.

3. Hence, on each mesh we should find an approximate solution of the equation $E'(\varepsilon_r)(x) = 0, x \in \Omega$. By (13) we hope to decrease the error via locally refining mesh in those regions, where the values of $|E'(\varepsilon_{r,h})(x)|$ are close to the maximal one.

For each new mesh we first linearly interpolate the function $\varepsilon_r^{glob}(x)$ on it. Since this function is computed on the globally convergent stage as a linear combination of finite elements of the initial mesh and these finite elements are piecewise linear functions, then subsequent linear interpolations on finer meshes do not change this function. On each mesh we iteratively update approximations $\varepsilon_{r,h}^n$ of the function $\varepsilon_{r,h}$. To do so, we use the quasi-Newton method with the classic BFGS update formula with the limited storage [25]. Denote

$$g^n(x) = \alpha(\varepsilon_{r,h}^n - \varepsilon_r^{glob})(x) - \int_0^T (u_{ht}\lambda_{ht})\left(x, t, \varepsilon_{r,h}^n\right) dt,$$

where functions $u_h\left(x, t, \varepsilon_{r,h}^n\right), \lambda_h\left(x, t, \varepsilon_{r,h}^n\right)$ are computed via solving state and adjoint problems (10), (11) with $\varepsilon_r := \varepsilon_{r,h}^n$. We stop computing $\varepsilon_{r,h}^n$ if either $||g^n||_{L_2(\Omega)} \leq 10^{-5}$ or norms $||g^n||_{L_2(\Omega)}$ are stabilized. For a given mesh, let $\varepsilon_{r,h} := \varepsilon_{r,h}^n$ be the last computed function on which we have stopped. Next, we compute the function $|E'(\varepsilon_{r,h})(x)|$ in (13) and consider all grid points in this mesh where

$$|E'(\varepsilon_{r,h})(x)| \geq \varkappa \max_{\overline{\Omega}} |E'(\varepsilon_{r,h})(x)|. \tag{14}$$

In (14) the maximum is taken over all grid points and $\varkappa \in (0, 1)$ is a tolerance number which should be chosen computationally. Next, we refine the mesh in neighborhoods of all grid points satisfying (14). The stopping criterion for the mesh refinement process is described in sub-subsection 6.2.1.

3   The Experimental Setup

For brevity below x denotes both a vector $x = (x, y, z) \in \mathbb{R}^3$ and the first component of this vector. It is always clear from the context what is what there. Our source/detectors configuration is schematically depicted on Figure 1. The source has generated an electro-magnetic (EM) wave. Only one component of the vector of the electric field was generated
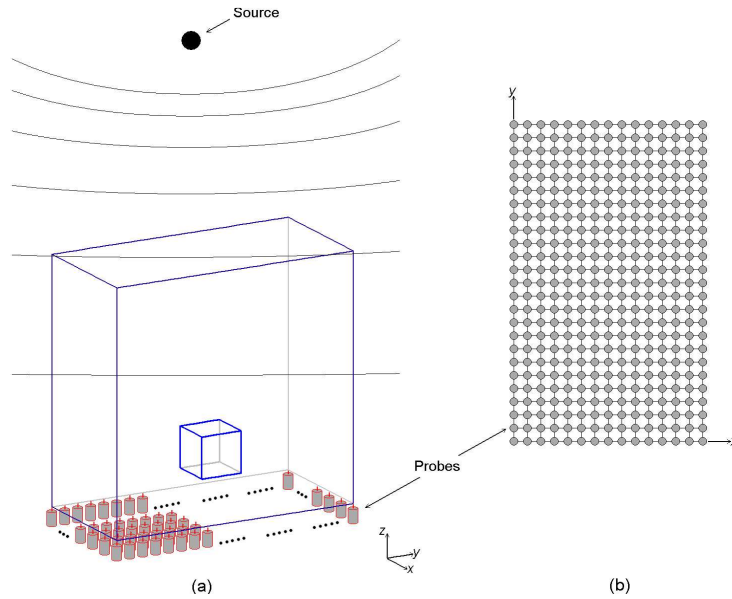
Figure 1: *Schematic diagram of the source/detectors configuration. a) The rectangular prism depicts our computational domain Ω source location outside of this prism was used. Tomographic measurements of the scattered time resolved EM wave were conducted on the bottom side of this prism. b) Schematic diagram of locations of detectors on the bottom side of the prism Ω. The distance between neighboring detectors was 10 mm.*

by our source. And only one component of this field was measured at the bottom side of the rectangular prism Ω depicted on Figure 1. We do not know which component was measured: we have only worked with the measured time dependent voltage in our computations. This prism is our computational domain Ω. It consisted of Styrofoam. Styrofoam is a material, whose relative permittivity $\varepsilon_r \approx 1$, i.e. the same as one in the air. The sizes of Ω were 240 mm×140 mm × 240 mm. Hence, sizes of front and back sides of the prism of Figure 1 are 240 mm× 240 mm and sizes of other four sides are 240 mm× 140 mm. The distance between the wave source and the top side of the domain Ω was 130 mm. The initializing pulse was 100 ps duration. Since the speed of the EM wave propagation in the air is 0.3 mm/ps, then it requires 433 ps $\approx$ 130/03 ps for this wave to travel from the source to the top boundary of Ω. Hence, it follows from (15) the wave did not yet reach the domain Ω during the 100 ps duration of this pulse. The initializing pulse was

$$f(t) = \begin{cases} \approx A\sin\left(\frac{\pi}{50}\tau\right), \text{ for } \tau \in (0, 100) \text{ ps}, \\ 0, \text{ for } \tau > 100 \text{ ps}, \end{cases} \tag{15}$$

where A is the amplitude. Our data processing procedure does not rely on a knowledge of A.

8

The time resolved signal was measured at some locations of the detector on the bottom side of the prism Ω, as indicated on Figure 1-b). On each detector location this signal was measured with the time interval of 20 picoseconds between two consecutive measurements for the total period of 12,300 picoseconds=12.3 nanoseconds. First, we were putting the detector at one location, sent the pulse and measured the time resolved scattering wave at this location. Next, we have moved the detector mechanically in a neighboring location and repeated the measurement, etc.. Hence, it is reasonable to assume in the mathematical model that the wave field was measured simultaneously at all those detectors. The distance between two neighboring locations of the detector was 10 mm, and so we have covered the entire bottom side of Ω by the grid of these locations of detectors. However, measurements was not conducted at other sides of this prism, see section 5.

We had two measurements at each detector location. First, we have measured the reference signal when the inclusion was not present. Second, we have measured the signal when the inclusion was present. In principle, our technique allows the measurement of the reference signal only at a few locations outside of the medium of interest: for the calibration purposes. The only reason why we have measured the reference signal for each location of the detector was that our current numerical implementation works only with the case when the initializing wave field is a plane wave. On the other hand, it was impossible to arrange a true plane wave in that experiment and so we had a spherical wave. Both here and in previous publications we have used the point source rather than the plane wave in (1), (2) only to obtain the asymptotic behavior (8), which actually follows from the construction of the fundamental solution of the hyperbolic equation in [29, 30]. In our computational practice we verify this asymptotic behavior numerically when working with plane waves, see subsection 7.2 of [9].

Our dimensionless computational domain Ω, the dimensionless distance $\widetilde{h}$ between two neighboring detectors and the dimensionless time t were [23]

$$\Omega = \{(x, y, z) \in [-2.4, 2.4] \times [-1.4, 1.4] \times [-2.4, 2.4]\}, \widetilde{h} = 0.2, \ t \in (0, 12). \quad (16)$$

Let P be the bottom side of the domain Ω in (16),

$$P = \{(x, y, z) : (x, y) \in [-2.4, 2.4] \times [-1.4, 1.4], z = -2.4\}. \quad (17)$$

4 Data Simulation

4.1 Data simulation

Since the computationally simulated data play an important role in our data pre-processing procedure, we outline here the solution of the forward problem for equation (1). Since it is practically impossible to solve the PDE (1) in the entire space $\mathbb{R}^3$, we have solved it in a larger rectangular prism $G = \{(x, y, z) \in [-3, 3] \times [-2, 2] \times [-5, 5]\}$. So, by (16) $\Omega \subset G$.

9

Our initializing plane wave was $v(t)$,

$$v(t) = \begin{cases} \sin(\omega t), & \text{for } t \in \left(0, \frac{2\pi}{\omega}\right), \\ 0, & \text{for } t > \frac{2\pi}{\omega}, \omega = 7. \end{cases} \tag{18}$$

Let ∂G_1 and ∂G_2 be respectively top and bottom sides of G and $\partial G_3 = \partial G \setminus (\partial G_1 \cup \partial G_2)$ be the rest of the boundary of G. We have numerically solved the following initial boundary value problem

$$\begin{aligned} \varepsilon_r(x)\, u_{tt} &= \triangle u, \quad \text{in } G \times (0,T), T = 12, \\ u(x,0) &= 0, \ u_t(x,0) = 0, \ \text{in } G, \\ \partial_n u\big|_{\partial G_1} &= v(t), \ \text{on } \partial G_1 \times (0, 2\pi/\omega], \\ \partial_n u\big|_{\partial G_1} &= -\partial_t u, \ \text{on } \partial G_1 \times (t_1, T), \\ \partial_n u\big|_{\partial G_2} &= -\partial_t u, \ \text{on } \partial G_2 \times (0,T), \\ \partial_n u\big|_{\partial G_3} &= 0, \ \text{on } \partial G_3 \times (0,T), \end{aligned} \tag{19}$$

In the case when data are simulated for the reference medium, we have in (19) $\varepsilon_r(x) \equiv 1$. We denote this solution as $u_1(x,t)$. Thus, in (19) the plane wave is initialized at the top boundary ∂G_1 for times $t \in (0, 2\pi/\omega]$ and propagates into G. First order absorbing boundary conditions [18] were used on the top boundary for $t \in (2\pi/\omega, T)$ as well as on the bottom boundary ∂G_2 for $t \in (0,T)$. The zero Neumann boundary condition was used on the rest of the boundary of the prism G. The latter boundary condition is used because the "pure" plane wave with $\varepsilon_r(x) \equiv 1$ satisfies this condition. The problem (19) was solved by the hybrid FEM/FDM method described in [13]. In this method, FDM is used outside of the domain Ω, i.e. in $G \setminus \Omega$, and FEM, is used inside of Ω. The step size in the overlapping region was $\widetilde{h} = 0.2$ which is the same as the distance between any two neighboring detectors.

4.2   Solving problems (10) and (11) in the adaptivity

Although the above theory says that we should solve forward (10) and adjoint (11) problems in the domain Ω, we actually solve both of them in larger domains. Namely, in our computations the problem (10) is solved in the domain G with boundary conditions (19). And the problem (11) is solved in such a part of the domain G which is above the bottom side P in (17) of the prism Ω, i.e. in the subdomain $G' = G \cap \{z > -2.4\}$. Let $P_{obs} = \{z = -2.4\} \cap G$. Then by (17) the rectangle $P \subset P_{obs}$. When solving the problem (11), we use the boundary condition $\partial_n \lambda\,|_{P_{obs}} = (g - u)\,|_{P_{obs}}$. Hence, we actually need to know the function $g(x,t)$ not only on the rectangle P but also on a wider rectangle P_{obs}. As to the rest of the boundary of the domain G', we use absorbing boundary conditions $\partial_n \lambda = -\partial_t \lambda$. We believe that the above theory of the adaptivity can be extended to this case, although we have not yet done this.

5 Data Pre-Processing

The main idea of this procedure is to *immerse* the experimental data in the computationally simulated ones. We have done this in three stages described in follow up sub-sections of this section. The third stage is new, whereas first two stages were described in [23]. The data pre-processing procedure provides us with the boundary data at $\partial \Omega$, which we use in our computations.

An important observation of our computational simulations was that, at least for times which are near of times of the first arrival of the EM wave, the bottom side P of Ω was the most sensitive part of $\partial \Omega$, to the presence of inclusions. This observation has saved us a lot of time when collecting our data. For this reason, we have prescribed to all points of $\partial \Omega \setminus P$ the same values as ones we got in computations of the forward problem (19) for the case $\varepsilon_r \equiv 1$, i.e. for the case of the air, which fills the medium outside of Ω.

a)   b)
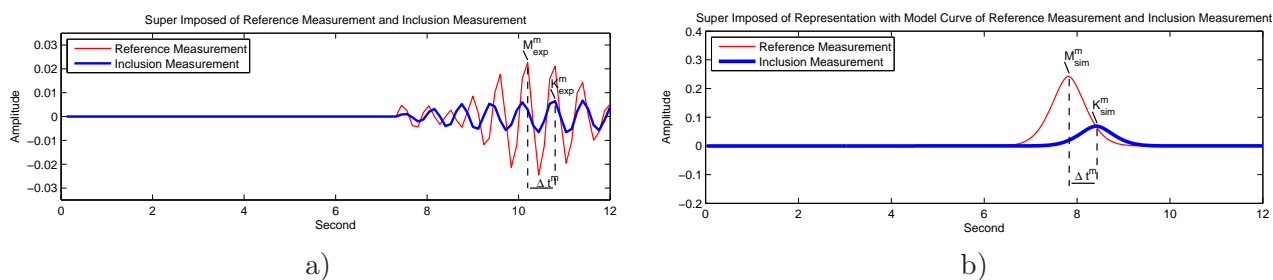
Figure 2: *This figure explains the idea of the first stage of data immersing in the time domain. We have intentionally set to zero the small amplitude fluctuations before that first burst. a) Resulting superimposed experimental curves. The red curve (thin) is for the reference signal and the blue curve (thick) is for the signal with a dielectric inclusion present, both at the same location $x_m \in P$ of the detector number m. b) The red curve (thin) displays computationally simulated data $u_{ref}(x_m, t)$. The blue curve (thick) $u_{incl}(x_m, t) = u_{ref}(x_m, t - \Delta t^m) K_{\exp}^m / M_{\exp}^m$ represents a sample of the immersed experimental data in the time domain at the same detector location $x_m \in P$. It is only the blue curve (thick) with which we work further. The red curve (thin) is displayed for the illustration purpose only.*

5.1   First immersing in the time domain (the first immersing stage)

Let $x_m \in P$ be the detector number m at the bottom side P of the prism Ω, see (17) for P. Samples of unprocessed experimental data can be found on Figure 2 of [23]. As in [23], we work with the first burst only. Figure 2-a) displays a sample of the first burst after a partial denoising via the Fourier transform, see details in [23]. We have decided to "immerse" our experimental data in the computationally simulated data using the following two peaks for each detector x_m :

1. The largest peak in the red curve (thin line, reference medium) with the peak value of $M_{\exp}^m$.

11

a) $\varepsilon_r^{(2,2)} = 1.25, n^{(2,2)} = 1.12$ b) $\varepsilon_r^{(4,2)} = 2.49, n^{(4,2)} = 1.58$ c) $\varepsilon_r^{(5,2)} = 3.9, n^{(5,2)} = 1.97$
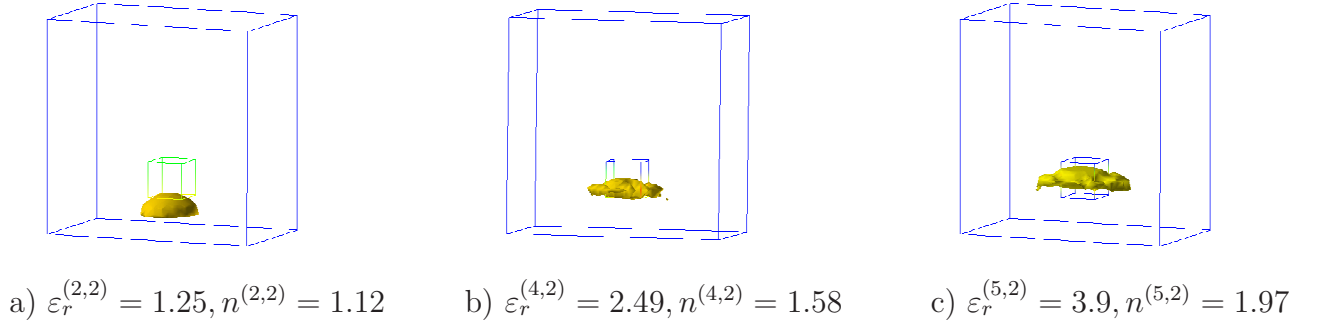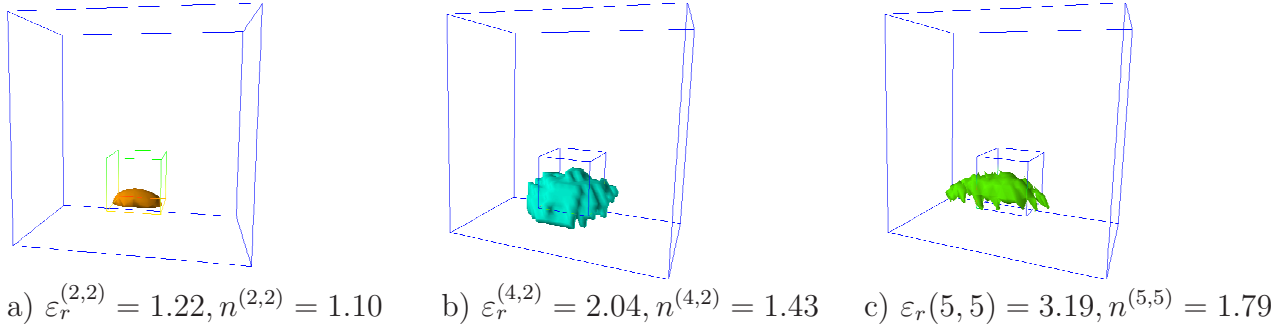
Figure 3: *Spatial distributions of iteratively computed dielectric constants $\varepsilon_r^{(n,k)}$ and refractive indexes $n^{(n,k)} = \sqrt{\varepsilon_r^{(n,k)}}$ for the Cube No. 1 (Table 1). The final image corresponds to $n^{(5,2)} := n_{glob} = 1.97$. See Table 2 for the reconstruction accuracy. Recall that refractive indices rather than dielectric constants are actually measured experimentally.*

2. The next peak after it in the blue curve (thick line, the medium with a dielectric inclusion present) with the peak value of $K_{\exp}^m$. This next peak was chosen because the presence of a dielectric inclusion results in a time delay of the EM wave, see (3).

Recall that the function $u_1(x,t)$ is the solution of the problem (19) with computationally simulated data for $\varepsilon_r \equiv 1$. Obviously $u_1\left(x^{(1)}, t\right) = u_1\left(x^{(2)}, t\right)$, $\forall x^{(1)}, x^{(2)} \in P$, $\forall t \in (0, T)$. Let $t := t_{ref}^{sim}$ be the time of the first arrival of the computationally simulated plane wave $u_1(x,t)$ at the plane P. In other words, for all $x \in P$ we have $u_1(x,t) = 0$ for $t < t_{ref}^{sim}$ and $u_1(x,t) > 0$ for such moments of time $t > t_{ref}^{sim}$ that are rather close to t_{ref}^{sim} with, see the reference curve on Fig. 2-b).

We point out that amplitudes of largest peaks of experimental curves for the reference medium were different for different detectors. This is because it was impossible to arrange experimentally the true plane wave for the reference medium. Experimentally we actually had a spherical wave. Nevertheless, we have "forced" it to be a plane wave via applying the first stage of our data immersing procedure.

Let $y = y_m^{ref}(t)$ be the experimentally measured curve at the detector $\{x_m\}$ for the reference medium, i.e. when the dielectric inclusion was not present. Let the above chosen largest peak of this curve is achieved at $\left\{t = t_m^{ref}\right\}$ and its value is $y_m^{ref}\left(t_m^{ref}\right) = M_{\exp}^m$. Let $y = y_m^{incl}(t)$ be the experimentally measured curve at the detector $\{x_m\}$ for the case when inclusion is present. We choose such a local maximum of the function $y = y_m^{incl}(t)$ which is achieved at the first point $\left\{t = t_m^{incl}\right\}$ which follows after the point $\left\{t = t_m^{ref}\right\}$, see Fig. 2-a). Let $y_m^{incl}\left(t_m^{incl}\right) = K_{\exp}^m$. So, $K_{\exp}^m$ is the value of the latter peak, see Figure 2-a). On all detectors we have observed that $K_{\exp}^m \leq M_{\exp}^m$. This is because the presence of dielectrics decreases the amplitude of the EM wave. We enforce

$$K_{\exp}^m := M_{\exp}^m, \text{ if } \frac{K_{\exp}^m}{M_{\exp}^m} \geq \frac{2}{3}. \tag{20}$$

12

a) $\varepsilon_r^{(2,2)} = 1.22, n^{(2,2)} = 1.10$ b) $\varepsilon_r^{(4,2)} = 2.04, n^{(4,2)} = 1.43$ c) $\varepsilon_r(5,5) = 3.19, n^{(5,5)} = 1.79$

Figure 4:   *Spatial distributions of iteratively computed dielectric constants $\varepsilon_r^{(n,k)}$ and refractive indexes $n^{(n,k)} = \sqrt{\varepsilon_r^{(n,k)}}$ for the Cube No. 2 (Table 2). The final image corresponds to $n^{(5,5)} := n_{glob} = 1.79$, which is only 4.5% error compared with the experiment, see Table 2. Recall that refractive indices rather than dielectric constants are actually measured experimentally.*

Now we are ready to immerse our experimental data in the computationally simulated data. Let $\Delta t_m = t_m^{incl} - t_m^{ref}$ be the time delay between two above chosen peaks, see Figure 2-a). Then we set

$$u_{incl}(x_m, t) = \frac{K_{\exp}^m}{M_{\exp}^m} u_1(x_m, t - \Delta t_m). \tag{21}$$

So, (21) is our *first immersed data in the time domain* for the detector number m. Figure 2-b) illustrates (21). By (20) and (21) if $K_{\exp}^m/M_{\exp}^m \geq 2/3$, then we set $u_{incl}(x_m, t) := u_1(x_m, t)$. After this data immersing, we use only the curve $u_{incl}(x_m, t)$ and do not use the curve for the reference medium anymore. We cannot rigorously justify our above decision to work with those peaks only. However, since our results of blind imaging in [23] were very accurate ones, then this justifies our purely intuitive choice.

5.2   The second stage of data immersing

Next, we apply the Laplace transform (7) to each function $u_{incl}(x_m, t)$ for nine values of $s \in [3.5, 7.5 w_{incl}(x_m, s)$ the Laplace transform of the function $u_{incl}(x_m, t)$. Let $\widetilde{w}_{incl}(x_m, s) = -s^{-2} \ln w_{incl}(x_m, s)$. Let $\overline{w}_{incl}(x, s)$ be the standard linear interpolation of the values $\{\widetilde{w}_{incl}(x_m, s)\}$ over the plane P. We have observed that the function $\overline{w}_{incl}(x, s)$ is very noisy with respect to x. Hence, we have applied a smoothing procedure to the function $\overline{w}_{incl}(x_m, s)$ with respect to $(x, y) \in P$ for each of those nine values of s. Specifically, we have used the *Lowess fitting procedure* in the 2D case, which we took from MATLABR 2009. We have obtained the function $\overline{w}_{smooth}(x, s)$. Let $w_1(x, s), x \in P$ be the Laplace transform of the function $u_1(x, t)$, i.e. for the case of the plane wave propagating in the air. Then we finally set for
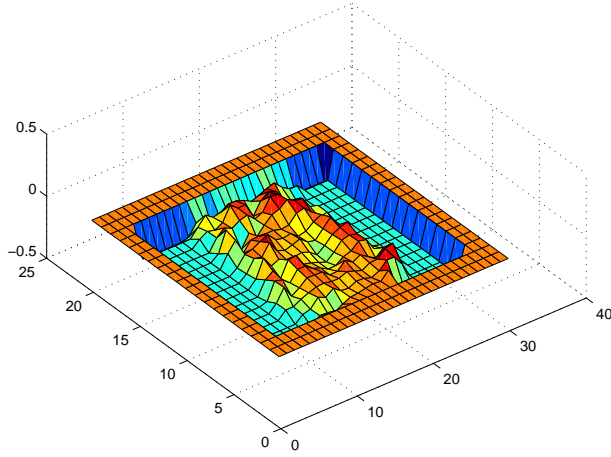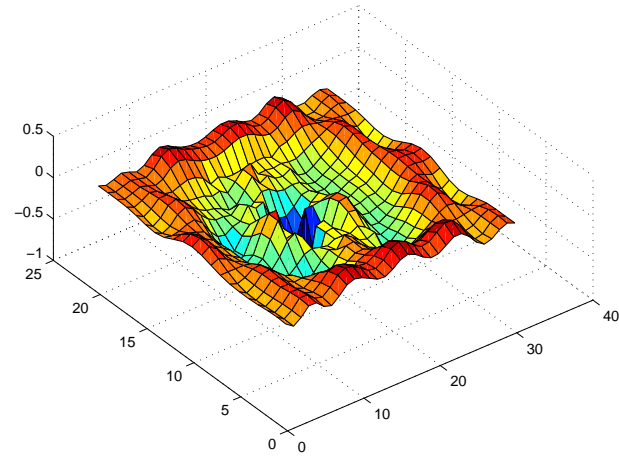
a) $t = 10.8$
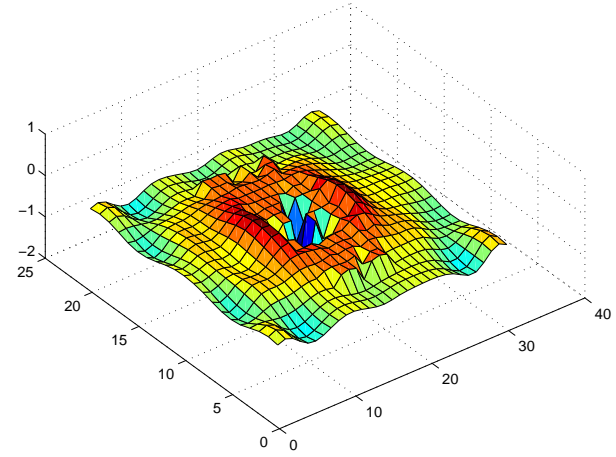
b) $t = 10.8$
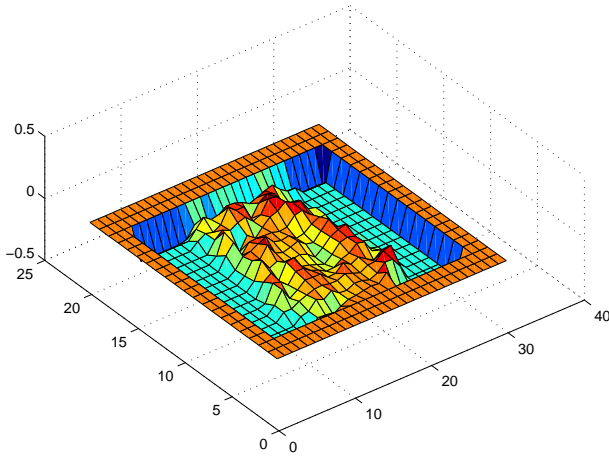
c) $t = 12.0$

d) $t = 12.0$

Figure 5: *a), c) Data for the cube No. 1 (Table 1) resulting after the first stage of the immersing procedure, i.e. this is the function $u_{incl}(x,t)$, $x \in P$. We immerse these data into the data obtained via the solution of the problem (19) for $\varepsilon_r(x) := \varepsilon_r^{glob}(x)$. However, this function is unknown for $x \in P_{obs} \setminus P$, whereas we need this knowledge for the adaptivity (subsection 4.2). Hence, immersed data are presented at P_{obs} with $\beta = 0.1$ in b), d). The coefficient $\varepsilon_r^{glob}(x)$ is the one computed by the globally convergent method for the cube No. 1, see Tables 2 and Fig. 3-c).*

14

each of those nine values of s

$$\overline{w}_{immers}(x,s) = \begin{cases} \overline{w}_{smooth}(x,s), & \text{if } \overline{w}_{smooth}(x,s) \geq 0.985 \max_{\overline{P}} \overline{w}_{smooth}(x,s), \\ -s^{-2}\ln w_1(x,s), & \text{otherwise,} \end{cases}$$

see Figure 5 in [23]. So, we use the function $\overline{w}_{immers}(x,s)$ to obtain Dirichlet boundary conditions for above mentioned elliptic equations of the globally convergent method (section 2).

5.3 Reconstruction by the globally convergent method

It was shown in [23] that first and second immersing stages of two previous subsections are sufficient for the globally convergent algorithm. Our dielectric abnormalities to be imaged were two wooden cubes, see Table 1. Let CL be the center line, i.e. the straight line which is orthogonal to the plane P and which passes through the source of EM waves (Figure 1). Then $CL = \{(x,y,z) : x = y = 0\}$. We test our two-stage numerical procedure on two sets of experimental data. So, the center of our first cube was on CL, and the center of the second cube was off CL by 0.2 in dimensionless coordinates, which is equivalent with 10 mm. Images are presented on Figures 3 and 4. One can see from Table 2 that the error of the reconstruction of refractive indices is a few percent. The same conclusion was drawn in [23]. At the same time, it is clear from Figures 3 and 4 that it is desirable to improve images of shapes of these cubes. And this is why we use the adaptivity technique on the second stage.

Cube number	Original sizes, mm	Dimensionless sizes	Dimensionless coordinates of centers
1	$40 \times 40 \times 40$	$0.8 \times 0.8 \times 0.8$	$(0,0,-1.2)$
2	$60 \times 60 \times 60$	$1.2 \times 1.2 \times 1.2$	$(0.2,0,-1.2)$

Table 1: *Sizes and coordinates of centers of two wooden cubes used in experiments*

Cube number	Computed $n := n_{glob} = \sqrt{\varepsilon_r^{glob}}$	Measured n, error	Comput. error
1	1.97	2.07, 11%	4.8%
2	1.79	1.71, 3.5%	4.5%

Table 2: *Computed refractive indices* $n := n_{glob} = \sqrt{\varepsilon_r^{glob}}$ *and ones directly measured by the Waveguide Method*

5.4 The third stage of data immersing

This stage is new, since it was not a part of [23]. The function $u_{incl}(x_m, t)$ obtained in (21) is very noisy with respect to $x_m \in P$, see for example Figures 5-a), c) for this function. We know this function only at the bottom side P of the rectangular prism Ω. However, it was pointed

15

out in subsection 4.2 that in order to solve the adjoint problem, we actually need to know this function on the bigger rectangle $P_{obs} = \{(x, y, z) : (x, y) \in [-3, 3] \times [-2, 2], z = -2.4\}$. So, since our experimental data were measured on a smaller rectangle P only, we need to complement them somehow on the set $P_{obs} \backslash P$. To do so, we have decided to solve the problem (19) with a certain coefficient ε_r: to complement the data on $P_{obs} \backslash P$. Let $\overline{u}(x, t)$ be this solution. Then we treat values of $\overline{u}(x, t)|_{P_{obs}}$ as a certain part of immersed boundary values $g|_{P_{obs}}$ when solving the adjoint problem (11). In other words, this solution provides us with a new piece of data at the entire rectangle P_{obs}. Hence, the question now is: *How to choose the coefficient ε_r in equation (19) for this third immersing stage?*

We have decided to take in equation (19) the coefficient $\varepsilon_r^{glob}(x)$, which was obtained on the globally convergent stage of our two-stage numerical procedure, see Figures 3 and 4 as well as Table 2. Let $U_{ref}(x, t)$ be the solution of the problem (19) with $\varepsilon_r(x) := \varepsilon_r^{glob}(x)$. Thus, we define our second immersed data in the time domain as

$$u_{immers}(x,t)|_{P_{obs}} = \begin{cases} u_{incl}(x, t), & \text{if } u_{incl}(x, t) \geq \beta \max_{\overline{P}}(u_{incl}(x, t)) \text{ and } x \in P, \\ U_{ref}(x, t), & \text{otherwise}, \end{cases} \quad (22)$$

where the function $u_{incl}(x, t)$ is the standard linear interpolation of values $u_{incl}(x_m, t)$ in (21) over the rectangle P. In particular, (22) implies that $u_{immers}(x,t) = U_{ref}(x, t)$ for $x \in P_{obs} \backslash P$. In (22) the parameter $\beta \in (0, 1)$ should be chosen in numerical experiments. This parameter characterizes the amount of information which we take from the first immersed experimental data in (21). Comparison of Figures 5-a), c) with Figures 5-b), d) shows that the third stage of data immersing helps not only to obtain the data for $x \in P_{obs} \setminus P$ (rather than for $x \in P$ only), but also to significantly decrease the noisy component of the data resulting from the first immersing stage. We also show numerically below (Figure 10) that the change of the parameter β in the wide range $\beta \in (0.1, 0.985)$ does not significantly affect imaging results.

Thus, we now got a "double use" of the solution obtained on the globally convergent stage. First, for the data immersing via (22). Second, as the starting point for the adaptivity technique.

6 Reconstruction Results

While Figures 3-c) and 4-c) display reconstruction results via the globally convergent stage, we present in this section refined results which were obtained on the adaptivity stage. As it was pointed out in the second Remark 2.2, the mesh refinement recommendation of (23) provides only an indication of those regions where mesh should be refined. However, it can also be refined in other places. Hence, when applying the adaptivity to the experimental data, we have developed a new procedure of mesh refinements, which consists of two stages, see subsections 6.2 and 6.3.

6.1 Some details of the numerical implementation of the adaptivity

Recall that by (14) we refine the mesh in all regions where

$$|E'(\varepsilon_{r,h})(x)| \geq \varkappa \max_{\overline{\Omega}} |E'(\varepsilon_{r,h})(x)|, \tag{23}$$

where $\varkappa = const \in (0,1)$ is the tolerance number of our choice. The choice of $\varkappa$ depends on concrete values of $|E'(\varepsilon_{r,h})(x)|$ and this should be done in numerical experiments. Below we take in (23) $\varkappa = 0.8$ for all computational meshes. Just as in [10, 11, 12], we have used a cut-off parameter B_{cut} on all refined meshes for the reconstructed coefficient $\varepsilon_{r,h}$. Namely, we took

$$\varepsilon_{r,h}(x) = \begin{cases} \varepsilon_{r,h}(x), & \text{if } |\varepsilon_{r,h}(x) - \varepsilon_{r,h}^{glob}(x)| \geq B_{cut}, \\ \varepsilon_{r,h}^{glob}(x), & \text{elsewhere.} \end{cases} \tag{24}$$

Our numerical experience of previous publications [10, 11, 12] has shown that it is important to use in the adaptive algorithm box constrains for the reconstructed coefficient via imposing that $1 \leq \varepsilon_{r,h}(x) \leq d$. While the inequality $\varepsilon_{r,h}(x) \geq 1$ follows from physics, see (3), we find a good estimate for the upper bound d on the basis of computed refractive indices from globally convergent part, i.e. on the basis of the second column of Table 2. Concrete values of B_{cut} and d can be found in subsections below.

6.2 Reconstruction results for the Cube No. 1

The function $\varepsilon_r^{glob}(x)$, which corresponds to Fig. 3-c), was taken as the starting point in adaptivity technique on all meshes, as well as the one generating the function U_{ref} in (22). We took in (24) $B_{cut} = 2$ for all refinements of the mesh. Since by Table 2 $\max \varepsilon_r^{glob}(x) = (1.97)^2 \approx 3.9$, we enforce that the coefficient $\varepsilon_r(x)$ belongs to the following set of admissible parameters $\varepsilon_r(x) \in C_M = \{1 \leq \varepsilon_r(x) \leq 4.4\}$.

### 6.2.1 The first stage of the mesh refinement

On this stage we refine mesh locally in the following two types of regions:

1. The one where we have the standard mesh refinement recommendation. That is, we refine mesh in all regions where (23) is fulfilled.

2. In addition, we refine mesh in those regions where the coefficient imaged on the globally convergent stage attains values which are sufficiently close to its maximal value. In other words, we refine mesh in all regions where $\geq \alpha \max_{r}^{glob}(x)$, where the parameter $(0,1)$ is chosen in numerical experiments. In our specific case of cube No.1 $\max_{\overline{\Omega}} \varepsilon_r^{glob}(x) = 3.9$. In all calculations below we took

$$\alpha = 0.2, \beta = 0.985, \gamma = 0.001, \tag{25}$$

where γ is the regularization parameter of the Tikhonov functional (9).
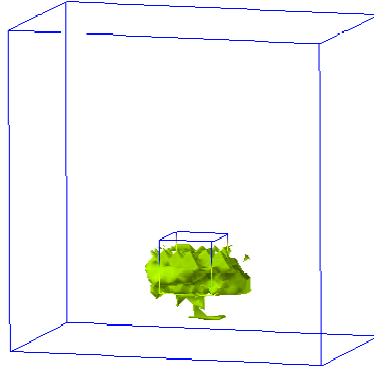
$$\varepsilon_{r,h} \approx 3.9, n_{glob} = \sqrt{\varepsilon_{r,h}} \approx 1.97$$

Figure 6: *The reconstruction result for the 1st stage of the adaptivity for the cube No. 1. Maximal values of the imaged coefficient are shown for the third refined mesh. The shape is not yet well reconstructed, although a comparison with Fig. 3-c) shows an improvement. The refractive index is reconstructed accurately (Table 2).*
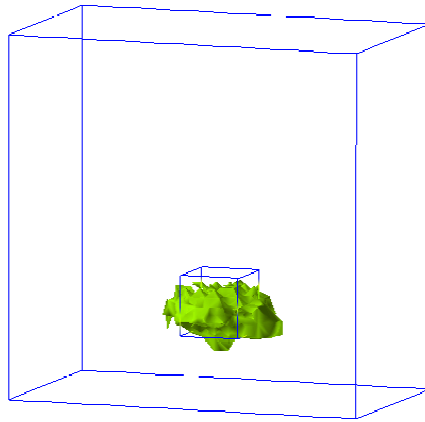
$$\varepsilon_{r,h} \approx 3.9, n_{glob} = \sqrt{\varepsilon_{r,h}} \approx 1.97$$

Figure 7: *The reconstruction result for the 2nd stage of the adaptivity for the cube No. 1. Thin lines (blue) indicate the correct cubical shape. Comparison with Fig. 6 shows an improvement of the image. The refractive index is reconstructed accurately (Table 2).*

First, we use the same coarse mesh as the one on the globally convergent stage. Just as in [10]-[12], we have not observed any improvement of the image. Next, we use adaptively locally refined meshes. Let $\Gamma_T = P_{obs} \times (0, T)$. To figure out the stopping criterion with respect to the mesh refinements, we proceed similarly with Table 2 of [10] and Table 1 of [11]. Namely, let $\varepsilon_{r,h}(x)$ be the approximation for the true coefficient $\varepsilon_r(x)$, which is obtained on a certain mesh, and $u := (x, t; \varepsilon_{r,h})$ be the corresponding solution of the forward problem (19). So, we analyze the behavior of computed L_2-norms of $\|u - u_{immers}\|_{L_2(\Gamma_T)}$. We have observed that these norms decrease with the number of mesh refinements. Next, this norm slightly increases on the 4$^{\text{th}}$ refinement. This is the same behavior as one in [10, 11]. Hence, we take the coefficient $\varepsilon_r(x)$ obtained after three mesh refinements as our final solution on the first stage of the adaptive algorithm. The resulting image is shown on Figure 6. Comparison of Figures 3-c) and 6 shows that the image of Fig. 6 is better than one of Fig. 3-c), whereas refractive indices are the same. However, the shape of the inclusion is not yet imaged well, although the size of the abnormality is computed rather well.

6.2.2 The second stage of the mesh refinement

One can derive from Fig. 6 that maximal values of the reconstructed coefficient are achieved in the subdomain Ω_1,

$$\Omega_1 = \{(x, y, z) : (x, y) \in [-0.5, 0.5] \times [-0.6, 0.6] \times [-1.4, -0.5]\}, \tag{26}$$

We now specify the last statement. Let $\overline{\varepsilon}_r(x)$ be the coefficient imaged on the first stage of the mesh refinement process. On the second stage we do not follow the conventional mesh refinement recommendation (23). Instead we refine the mesh locally only in those regions where

$$x \in \left\{ \overline{\varepsilon}_r(x) \geq \alpha \max_{\overline{\Omega}} \overline{\varepsilon}_r(x) \right\} \cap \Omega_1., \tag{27}$$

where α is taken from (25). This method provides a more regular refinement of the computational mesh. Hence, we hope to image a better shape of the inclusion. We have used parameters α, β, γ from (25). The same stopping criterion for the number of mesh refinements as one above was used. Figure 7 displays the final image after four mesh refinements. Comparison of Figs. 7 and 6 shows an improvement of the image due to the second stage of the adaptivity.
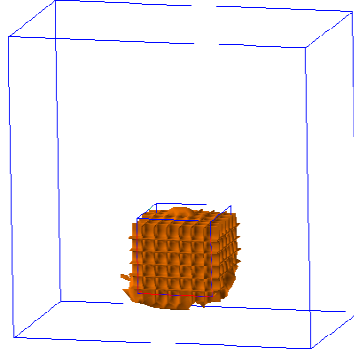
6.3 Reconstruction results for the Cube No. 2

We now apply the above adaptive two-stage technique to reconstruct the Cube No. 2 of Table 1. In doing so, we again get the first guess from the globally convergent method, see Fig. 4-c) and Table 2. Because of Table 2, we consider the following set of admissible parameters $\varepsilon_r(x) \in C_M = \{1 \leq \varepsilon_r(x) \leq 3.3\}$. Let j be the number of iterations in the quasi-Newton method on the 1$^{\text{st}}$ stage of the adaptivity. On all refined meshes we have chosen the cut-off parameters in (24) as: $B_{cut} = 0.91$ for $j = 1, 2$, for $j = 3, B_{cut} = 1.1$ and $B_{cut} = 2$ for $j > 3$.
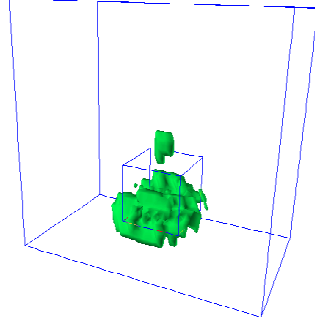
$$\varepsilon_{r,h} \approx 2.52, n_{glob} = \sqrt{\varepsilon_{r,h}} \approx 1.59$$

Figure 8: *The reconstruction result for the 1st stage of the adaptivity for the cube No. 2. Only maximal values of the imaged coefficient are shown for the 3rd refined mesh. The shape of the final imaged coefficient is better than one on Fig. 4-c). However, the imaged refractive index is lowered by about 19% compared with the imaged on the globally convergent stage.*

$$\varepsilon_{r,h} \approx 3.0, n_{glob} = \sqrt{\varepsilon_{r,h}} \approx 1.73$$

Figure 9: *The final reconstruction result for the cube No. 2. Only maximal values of the computed coefficient are displayed. The imaged coefficient $\varepsilon_r(x) = 1$ outside of these images. All three components: shape, location and refractive index are imaged with a very good accuracy.*

6.3.1   The first stage of the mesh refinement

As in the case of cube No. 1, the use of the same mesh as one in the globally convergent method, did not lead to an improvement of the image. Again, just as in the case of the first cube, we refine the mesh in all regions where the inequality (23) with $\varkappa = 0.8$ is valid, as well as in all regions where $\varepsilon_r^{glob}(x) \geq \alpha \max_{\overline{\Omega}} \varepsilon_r^{glob}(x)$. We have used parameters (25) as well as the same stopping criterion for the number of mesh refinements as one in sub-subsection 6.2.1. Because of this criterion, we have stopped on the 3th mesh refinement. The final image of the first stage of the adaptivity is displayed on Fig. 8. Comparing this image with one on Fig. 4-c) and with Table 2, we observe a slight improvement of the imaged shape while the value of the refractive index has decreased by about 19%. In addition, we observe that we have actually obtained two disconnected imaged inclusions.

6.3.2   The second stage of the mesh refinement

We use the same procedure as one for the first cube. First, we have to figure out an analog of the domain Ω_1 in (26). To define upper and lower boundaries for the vertical coordinate z of the subdomain of local mesh refinements, we have decided to use again the information obtained on the globally convergent stage. We see on Fig. 4-c) that, unlike Fig. 8, we have only a single rather than two inclusions. Hence, we have decided to refine mesh, in terms of the vertical coordinate z as follows:

1. The top boundary z_{top} should be slightly below the low boundary of the small imaged inclusion of Fig. 8.

2. The low boundary z_{low} should be slightly below the bottom of the larger imaged inclusion of Fig. 8.

3. Boundaries with respect to horizontal coordinates (x, y) of the mesh refinement subdomain were determined from the criterion $\overline{\varepsilon}_r(x) \geq \alpha \max_{\overline{\Omega}} \overline{\varepsilon}_r(x)$ for values of $\overline{\varepsilon}_r(x)$, which is similar with (27). Consider the subdomain $\Omega_2 \subset \Omega$, where

$$\Omega_2 = \left\{ (x, y, z) : (x, y) \in [-0.6, 0.6] \times [-0.6, 0.6] \times [-1.8, -0.8] \right\}.$$

So, we refine the mesh, using the criterion (27), in which Ω_1 is replaced with Ω_2.

The same stopping criterion for the number of mesh refinements as one in sub-subsection 6.2.1 was used. Thus, we have concluded that the 3rd mesh refinement should be the final one. The resulting image is displayed on Fig. 9. A very accurate reconstruction of all three components of the Cube No. 2: shape, location and refractive index is evident.

6.4   Sensitivity to parameters β and γ

To investigate the sensitivity of our images to the choice of the regularization parameter γ in the Tikhonov functional (9), as well as to the parameter β in (22), we have performed further testing for cube No. 2 with different values of β and γ. Results are displayed on Figure 10. One can observe that the value of the regularization parameter γ does not impact reconstruction results significantly. One can also see that images for $\beta = 0.985$ and $\beta = 0.5$

Test	nr elements in mesh	$\|u\|_{\Gamma_T} - g\|_{L_2(\Gamma_T)}$	$n = \sqrt{\varepsilon_r}$	Measured $n = \sqrt{\varepsilon_r}$
1	62902	0.0635991	1.73	1.71
2	86352	0.0577953	1.73	1.71
3	50158	0.0317876	2.0	2.07
4	61368	0.025447	2.0	2.07

Table 3: $\|u\|_{\Gamma_T} - g\|_{L_2(\Gamma_T)}$ *together with comparison of values of refractive indexes for all tests on finally adaptively refined meshes. Here* $\Gamma_T = P_{obs} \times (0, T)$.

are almost the same, including imaged values of the refractive index. Surprisingly, images for the case $\beta = 0.1$ also look almost the same as ones for $\beta = 0.985$ and $\beta = 0.5$. However, values of the refractive index for $\beta = 0.1$ are lowered by about 10%. Hence, we conclude from Fig. 10 that our procedure is quite stable with respect to parameters β and γ.

6.5 Verification for the Cube No. 1

We have compared our imaging result for Cube No. 1 with computational simulations. To do so, we have computed the data for the forward problem for exactly the same cube as No. 1 in Table 1. We took $\epsilon_r = 4$ inside of this simulated cube. However, we have replaced $\omega = 7$ with $\omega = 14$ in (18) and (19), since this corresponds to the twice smaller dimensionless wavelength $2\pi/\omega$ in computational simulations. So, we have conjectured that having a two times lesser wavelength would result in a better image for the Cube No. 1. Indeed, with $\omega = 7$ the dimensionless wavelength in simulated data is 0.897, which is bigger than the dimensionless size 0.8 of the side of the first cube (Table 1). On the other hand, $\omega = 14$ gives us the dimensionless wavelength of $0.45 < 0.8$. Note that the dimensionless wavelength size of the side of the Cube No. 2 is $1.2 > 0.897$. We recall here the classical Rayleigh principle.

We have applied the same procedure as above to the computationally simulated data. The resulting image is displayed on Fig. 11-a). One can observe a very good quality of this image from synthetic data. Next, we have applied the same procedure as above to the experimental data for the Cube No. 1 with the single difference that we now have used $\omega = 14$ instead of the previous $\omega = 7$. The resulting image is displayed on Fig. 11-b). One can observe a significant improvement compared with Figure 7. Hence, our conjecture about ω was partially materialized for the case of experimental data. Still, however, the image on Fig. 11-b) is not as good as the one for Cube No. 2 on Fig. 9.

7 Discussion

In this paper we have continued our work on experimental data of [23]. While only locations and refractive indices of dielectric abnormalities were accurately computed in [23], we now complement those by reconstructions of shapes. As a result, the shape of the Cube No. 2 is reconstructed with an excellent accuracy (Fig. 9). Furthermore, it was shown that our
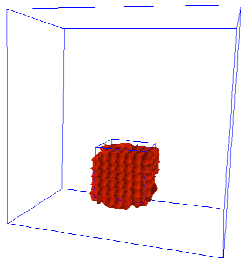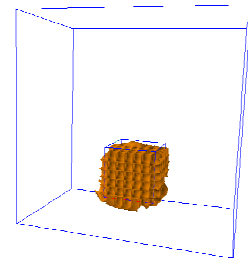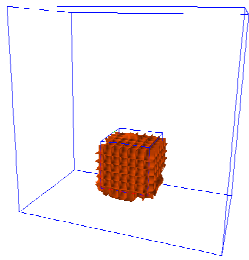
a) $\gamma = 0.001, \beta = 0.985$
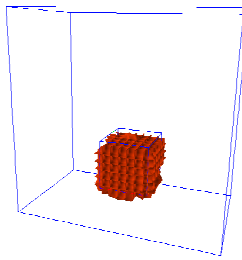$\varepsilon_{r,h} \approx 3.2, n_{glob} = 1.79$
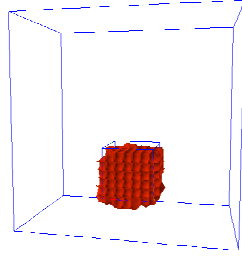
b) $\gamma = 0.01, \beta = 0.985$
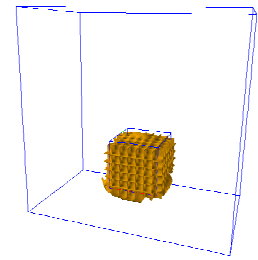$\varepsilon_{r,h} \approx 3.2, n_{glob} = 1.79$

c) $\gamma = 0.1, \beta = 0.985$
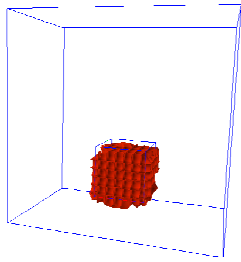$\varepsilon_{r,h} \approx 3.2, n_{glob} = 1.79$

d) $\gamma = 0.001, \beta = 0.5$
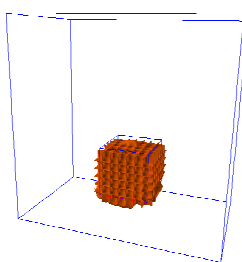$\varepsilon_{r,h} \approx 3.1, n_{glob} = 1.76$

e) $\gamma = 0.01, \beta = 0.5$
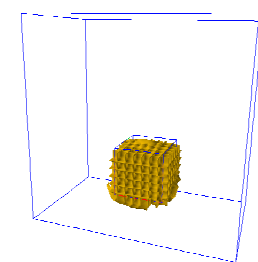$\varepsilon_{r,h} \approx 3.1, n_{glob} = 1.76$

f) $\gamma = 0.1, \beta = 0.5$
$\varepsilon_{r,h} \approx 3.0, n_{glob} = 1.73$

g) $\gamma = 0.001, \beta = 0.1$
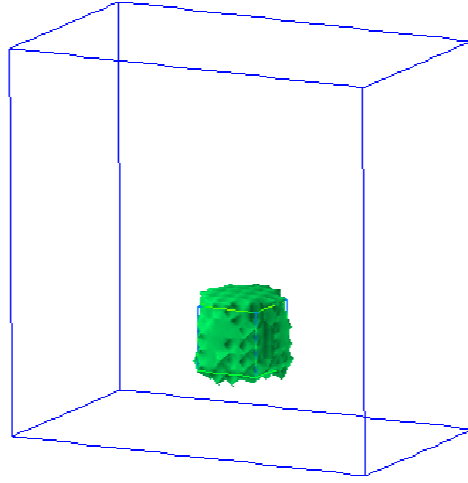$\varepsilon_{r,h} \approx 2.4, n_{glob} = 1.55$

h) $\gamma = 0.01, \beta = 0.1$
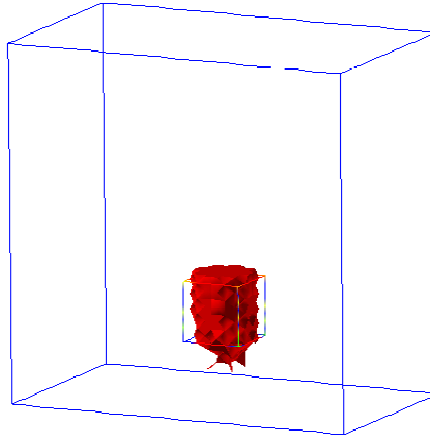$\varepsilon_{r,h} \approx 2.4, n_{glob} = 1.55$

i) $\gamma = 0.1, \beta = 0.1$
$\varepsilon_{r,h} \approx 2.4, n_{glob} = 1.55$

Figure 10: *Final reconstruction results for cube No. 2 with varying parameters β and γ. Lines (blue) indicate the correct cubical shape. Maximal values of the imaged coefficient are displayed. The computed value of the coefficient outside of imaged inclusions is 1.*

a) $\varepsilon_{r,h} \approx 4.09, n_{glob} = \sqrt{\varepsilon_{r,h}} \approx 2.02$

b) $\varepsilon_{r,h} \approx 4.2, n_{glob} = \sqrt{\varepsilon_{r,h}} \approx 2.05$

Figure 11: *a) The image of computationally simulated cube No. 1 from computationally simulated data with $\omega = 14$ in (18) and (19). b) The image of cube No. 1 from experimental data with $\omega = 14$ in (18) and (19). The same imaging procedure as above was applied. Compared with Fig. 7, a significant improvement is observed. Still, however, the image of the shape is not as good as the one for Cube No. 2 on Fig. 9.*

technique is quite stable with respect to some critical parameters which we choose in the reconstruction process (Fig. 10). The shape of the smaller Cube No. 1 was also reconstructed well (Fig. 11-b)), although the accuracy is not as good as the one of Cube No. 2. Just as in [23], refractive indices are imaged with a very good accuracy in both cases.

The difference of qualities of images of our two cubes might likely be attributed to the classical Rayleigh principle. Indeed, the original wavelength λ_{em} of the EM wave in our experimental data was $\lambda_{\mathrm{em}} = 3cm$. On the other hand, sizes of sides of Cubes No. 1 and No. 2 were respectively $4cm = 1.33\lambda_{\mathrm{em}}$ and $6cm = 2\lambda_{\mathrm{em}}$ (Table 1). Hence, we conjecture that the shape of the Cube No. 2 was imaged better than the one of Cube No. 1 because our experimental data had $3cm$ wavelength "inscribed" in them. This question needs to be investigated further.

Compared with [23], the main new element here is that we have complemented the globally convergent method by the adaptivity technique. In addition, we have complemented the traditional rule of mesh refinements by broader non-traditional ones, thus coming up with a two-stage mesh refinement procedure. Two other important features of these studies are:

1. The use of the solution obtained on the globally convergent stage is *crucial* for obtaining above results via the adaptivity. At least for the case of our experimental data the adaptivity does not work without the availability of this solution.

2. Our studies have consistently demonstrated that all analytical and numerical conclusions derived in our previous publications for computationally simulated data [9]-[12] were confirmed on experimental data.

Some discrepancies between our mathematical model and the reality are evident. It is well known that equation (1) cannot be derived from the Maxwell's system for the 3-D case if $\varepsilon_r \neq const$. In addition, we are not aware which of three components of the electric field was measured in experiments: we only knew that the time-resolved voltage was measured. Thus, we call (1) a *simplified* mathematical model of our process. A possible explanation why everything still works well is that the data immersing procedure "enforces" our data to be "good" for equation (1). A more complete investigation of this issue with the use of the full Maxwell's system is worthy to pursue. Since all three components of the electric field should be measured (rather than the current one), a significant technical obstacle on this path is that more experimental data should be collected, which is quite expensive. On the other hand, comparison of Fig. 11-a) with Fig. 11-b) indicates that a less expensive investigation of this issue on synthetic data only might be incomplete.

Another discrepancy is that in our globally convergent algorithm we need a certain asymptotic behavior of the Laplace transform of the function u, which can be derived from results of [29, 30], see (8) and Lemma 2.1 in [9]. In particular, that lemma requires at least the C^2-smoothness of the coefficient $\varepsilon_r(x)$. We verify that asymptotic behavior computationally, see subsection 7.2 [9]. However, the smoothness assumption of the function $\varepsilon_r(x)$ is obviously violated at the boundaries of our two cubes, which were used in experiments. More discrepancies can be derived from data immersing procedures described above. It might well take years to figure out how to handle all these discrepancies.

In summary, it is rather surprising that, despite all these discrepancies, results of this

publication as well as results of blind testing of [23] consistently demonstrate a very good reconstruction accuracy. We believe that the latter validates our simplified mathematical model as well points towards the robustness of our two-stage numerical procedure.

<div align="center">**Acknowledgments**</div>

References

[1] Ainsworth M and Oden J T 2000 *A Posteriori Error Estimation in Finite Element Analysis* (New York: Wiley)

[2] Alexeenko N V, Burov V A and Rumyantseva O D 2008 Solution of three-dimensional acoustical inverse problem: II. Modified Novikov algorithm *Acoust. Phys.* **54** 407-419

[3] Ammari H, Iakovleva E and Lesselier D 2007 Music-type electromagnetic imaging of a collection of small three dimensional inclusions *SIAM J. Sci.Comp.* **29** 674-709

[4] Beilina L and C. Johnson C 2001 A hybrid FEM/FDM method for an inverse scattering problem. In *Numerical Mathematics and Advanced Applications - ENUMATH 2001.* Springer-Verlag.

[5] L. Beilina and C. Johnson, A posteriori error estimation in computational inverse scattering, *Mathematical Models and Methods in Applied Sciences*, 15, 23-37, 2005.

[6] Beilina L 2003 Adaptive finite element/difference method for inverse elastic scattering waves, *Appl. Comput. Math.*, **2** 119-134.

[7] Beilina L 2010 Adaptive Finite Element method for a coefficient inverse problem for the Maxwell's system, *Applicable Analysis*, to appear.

[8] Beilina L and Clason C 2006 An adaptive hybrid FEM/FDM method for an inverse scattering problem in scanning acoustic microscopy *SIAM J. Sci. Comp.* **28**, 382-402

[9] Beilina L and Klibanov M V 2008 A globally convergent numerical method for a coefficient inverse problem, *SIAM J. Sci. Comp.* **31** 478-509

[10] Beilina L and Klibanov M V 2010 Synthesis of global convergence and adaptivity for a hyperbolic coefficient inverse problem in 3D *Inverse and Ill-posed Problems* **18** 85-132

[11] Beilina L and Klibanov M V 2010 A posteriori error estimates for the adaptivity technique for the Tikhonov functional and global convergence for a coefficient inverse problem *Inverse Problems* **26** 045012

[12] Beilina L, Klibanov M V and Kokurin M Yu 2010 Adaptivity with relaxation for ill-posed problems and global convergence for a coefficient inverse problem *Journal of Mathematical Sciences,* Springer, **167** 279-325

[13] Beilina L, Samuelsson K and Åhlander K 2001 Efficiency of a hybrid method for the wave equation. In *International Conference on Finite Element Methods*, Gakuto International Series Mathematical Sciences and Applications. Gakkotosho CO., LTD

[14] Belishev M I 1997 Boundary control in reconstruction of manifolds and metrics (the bc method) *Inverse Problems* **13** R1-R45

[15] Belishev M I and Gotlib V Yu 1999 Dynamical variant of the bc-method: theory and numerical testing *J Inverse and Ill-Posed Problems* **7** 221-240

[16] Burov V A, Morozov S A and Rumyantseva O D 2002 Reconstruction of fine-scale structure of acoustical scatterers on large-scale contrast background, *Acoust. Imaging* **26** 231-238

[17] Engl H W, Hanke M and Neubauer A 2000 *Regularization of Inverse Problems* (Boston: Kluwer Academic Publishers)

[18] Engquist B and Majda A 1977 Absorbing boundary conditions for the numerical simulation of waves *Math. Comp.* **31** 629-651

[19] Griesbaum A, Kaltenbacher B and Vexler B 2008 Efficient computation of the Tikhonov regularization parameter by goal-oriented adaptive discretization *Inverse Problems* **24** 025025

[20] Grinevich P G 2000 The scattering transform for the two-dimensional operator with a potential that decreases at infinity at fixed nonzero energy *Russ. Math. Surv.* **55** 3-70

[21] Klibanov M V and Timonov A 2004 *Carleman Estimates for Coefficient Inverse Problems and Numerical Applications* (Utrecht, The Netherlands: VSP)

[22] Klibanov M V 1991 Inverse problems and Carleman estimates, *Inverse Problems* **8** 575–596

[23] Klibanov M V, Fiddy M A, Beilina L, Pantong N and Schenk J, Picosecond scale experimental verification of a globally convergent numerical method for a coefficient inverse problem, *Inverse Problems*, 26, 045003, 2010.

[24] Mueller J and Siltanen S 2003 Direct reconstructions of conductivities from boundary measurements *SIAM J. Sci. Comp.* **24** 1232-1266

[25] Nocedal J 1991 Updating quasi-Newton matrices with limited storage, *Mathematics of Comp.* **35** 773–782

[26] Novikov R G 1988 Multidimensional inverse spectral problem for the equation $-\triangle\psi + (v(x) - Eu(x))\psi = 0$ *Functional Analysis and Its Applications* **22** 11-22

[27] Novikov R G 1992 The inverse scattering problem on a fixed energy level for the two-dimensional *Schrödinger operator*, *J. Func. Anal. and Its Applications* **103** 409-463

[28] Repin S I 2008 *A Posteriori Estimates for Partial Differential Equations* (Berlin: de Gruiter)

[29] Romanov V G 1986 *Inverse Problems of Mathematical Physics* (Utrecht, The Netherlands: VNU)

[30] Romanov V G 2009 On smoothness of a fundamental solution to a second order hyperbolic equation, *Siberian Math. J* **50** 700-705

[31] Tikhonov A N, Goncharsky A V, Stepanov V V and Yagola A G 1995 *Numerical Methods for the Solution of Ill-Posed Problems* (London: Kluwer)

[32] Yamamoto M 2009 Carleman estimates for parabolic equations and applications *Inverse Problems* **25** 123013